

## Comparison of high spatial resolution stereo-PIV measurements in a turbulent boundary layer with available DNS dataset

S. Herpin<sup>1,2</sup>, C. Y. Wong<sup>1</sup>, J.-Ph. Laval<sup>2</sup>, M. Stanislas<sup>2</sup>, and J. Soria<sup>1</sup>

<sup>1</sup>Department of Mechanical Engineering  
MONASH University, VIC 3800 Australia (LTRAC)

<sup>2</sup>Laboratoire de Mécanique de Lille  
Ecole Centrale de Lille, Cité Scientifique, 59655 Villeneuve d'Ascq cedex, France

### Abstract

In the present contribution, the aptitude of Stereoscopic Particle Image Velocimetry (SPIV) and of Direct Numerical Simulations (DNS) to investigate coherent structures of near wall turbulence is evaluated. For this purpose, the general properties and constraints of the two techniques are first reviewed. Then, data obtained from stereo-PIV experiments in a boundary layer and DNS in a channel flow are considered. Some statistics of the velocity fields are computed, and the results obtained from the two approaches compared.

### Introduction

Near wall turbulence is a key point for the improvement of numerical modeling and of primary importance for the aeronautics and car industry. To understand such a complex phenomenon, the study of simple canonical wall-bounded flows is of fundamental interest. Recently, new tools such as Particle Image Velocimetry (PIV) and Direct Numerical Simulation (DNS) have given access to quantitative spatial information in such flows. The complementary use of experimental data and of numerical data to investigate coherent structures of near wall turbulence is certainly very promising. However, the two techniques are subject to specific constraints and shortcomings. As a consequence some of the properties of PIV and DNS datasets (type of flow, spatial resolution...) are quite different, and can influence the results of a comparative analysis of the data.

### Boundary layer flow vs Channel flow

The three canonical wall-bounded turbulent flows usually considered to investigate near-wall turbulence are boundary layer flows, channel flows, and pipe flows. Whereas various experimental studies have been dedicated to all three, the vast majority of DNS reported in the literature have been performed in channel flows. The main reason is that the numerical boundary conditions are straightforward to implement in channel flows: no-slip boundary conditions are applied at the bottom wall and at the top wall, and the homogeneity of the flow in both  $x$  and  $z$  allows periodicity and hence, Fourier expansion to be used in those directions. In the present contribution, the DNS dataset comes from a simulation of a channel flow, whereas the experimental one is a boundary layer flow. These two wall-bounded flows present the following differences:

- the channel flow is homogeneous in the streamwise direction, while the boundary layer develops in the flow direction,
- in channel flows, there is a favorable pressure gradient, whereas flat plate boundary layer flows have a zero pressure gradient and,
- the boundary layer is subject to intermittency with the outer flow.

Pope [7] indicates that their near wall behavior is fairly similar, but that the so-called "defect-law" of the outer region are different. Indeed, the deviation of the mean longitudinal velocity profile from the log law in the outer region appears to be much smaller for the channel than for the boundary layer. As far as the impact on coherent structures is concerned, the population of prograde and retrograde spanwise vortices for a boundary layer and a channel flow have been experimentally investigated by Wu et al [12]. The boundary layer and the channel gave similar results, with the exception of the region  $y/\delta > 0.45$  where a significantly larger fraction of retrograde vortices was found in the channel flow, presumably under the influence of the upper wall.

### Spatial dynamic range of the 2 techniques

The spatial dynamic range of the measurement technique is of primary importance when it comes down to the study of coherent structures. Indeed, these structures are present in a wide range of size, that depends on the Reynolds number of the flow. The spatial dynamic range of Particle Image Velocimetry has been studied in great detail by Adrian [4], Soria [20] and Foucaut et al [3], and summarised in [1]. Briefly, the spatial dynamic range of PIV is limited at low wavenumbers by the size of the camera CCD array, and at the high wavenumbers by the Interrogation Window (IW) size as well as the noise of the measurements. Even with an up-to-date PIV interrogation software and careful experimental procedure, one can only hope to reduce the IW size and the measurement noise by a limited amount. The spatial dynamic range of the experiment is then given by the size of the camera CCD array. A compromise often has to be made between the size of the field of view and the spatial resolution. This has been confirmed by a literature survey in [1] on recent PIV experiments.

The problematic for DNS is somewhat different, as the successful implementation of the simulation relies on the very fact that all the relevant scales are resolved within the computational domain [11]. For instance, the vast majority of DNS of channel flow make use of spectral methods in the streamwise and spanwise directions, and therefore impose periodic boundary conditions at the borders of the domain. For this approach to be valid, the computational domain must be large enough so the largest structures of the flow are not constrained by this domain. A usual procedure consist in checking that the two points correlations do decay to nearly zero within half of the domain. On the other hand, the mesh has to be fine enough to resolve the smallest scales of the flow, i.e. the Kolmogorov scale  $\eta$ . However, Moin [13] points out that this requirement is too stringent, as the resolution should only be such that most of the dissipation is captured. The requirements also vary with the choice of the numerical scheme : spectral methods have proved more accurate and efficient. The minimal resolvable lengthscale usually needs to be  $O(\eta)$ . A direct consequence is that the mesh step in the wall-normal direction is a function of the wall distance. To

summarise, the spatial dynamic range of DNS is determined by the range of scales to be resolved in the flow. Even with today's considerable supercomputer power, the DNS is still restricted to low Reynolds number turbulent channel flow.

An interesting study can be found in Saikrishnan et al [19] on the spatial resolution of the two techniques, with emphasis on averaging effect of the interrogation window in the PIV technique. A set of dual-plane PIV data, a set of DNS data at similar Reynolds number conditions, and the same set of DNS data but locally averaged to mimic the effect of the PIV interrogation window and of the laser sheet thickness were compared. The RMS values of the velocity components and vorticity were quantified and the vortex core angle distribution studied for the three datasets.

### Constraints on the number of 'independent' realisations

The number of instantaneous velocity fields acquired and their degree of correlation in time is of interest when a statistical analysis of the data is to be undertaken: the higher the number of independent samples, the better the convergence of the statistical quantities. This characteristic of the dataset is fixed by the experimental and by the numerical constraints that apply on the technique. As far as the experiments are concerned, the only limitation is given by the storage space and by the difficulty to maintain constant experimental conditions (temperature of the fluid...) over a long time. Nowadays PIV datasets easily feature 2000 to 4000 velocity fields per experiment. On the side of DNS, a more stringent constraint arises in the form of limited computational power, coupled to the necessity to satisfy the CFL condition for the time advancement of the simulation. This issue have been discussed in Moin and Mahesh [13], and in Jimenez [15]. In brief, the CFL condition is derived from numerical stability requirements and restricts the simulation to small time steps  $dt$ , function of the mesh size and of the local velocity of the flow. For turbulent wall-bounded flows, the mesh is typically very fine in the near wall region, and a small  $dt$  has to be used. Consequently, a high degree of correlation exists between consecutive velocity fields, and the DNS is usually computed over a limited physical time. The number of available independent realisations is therefore typically several order of magnitude higher for SPIV experiments than for DNS. The practical implications of this feature for the computation of statistics on the two datasets studied in the present contribution will be further discussed in section 3.

### Experimental and Numerical database

The database under consideration in the present contribution consist of instantaneous velocity fields from stereo-PIV measurements conducted in the LTRAC laboratory and of Direct Numerical Simulations from Lille. This section gives a presentation of those two datasets. In the following,  $x, y, z$  and subscripts 1,2,3 refer respectively to the streamwise, wall-normal and spanwise directions.

### Experimental procedure

The experimental data consist of 3C-2D instantaneous velocity fields measured in the turbulent boundary layer developing in the LTRAC water-tunnel. An extensive description of the setup can be found in Herpin et al [1] and [2]. The main points of the experimental procedure will be briefly described.

The measurements are taken in a streamwise wall-normal plane of a turbulent boundary layer at about  $Re_\theta = 2200$  with 4 PCO 4000 cameras arranged in 2 stereo systems aligned in the streamwise direction. A schematic of the setup is given in figure 1.

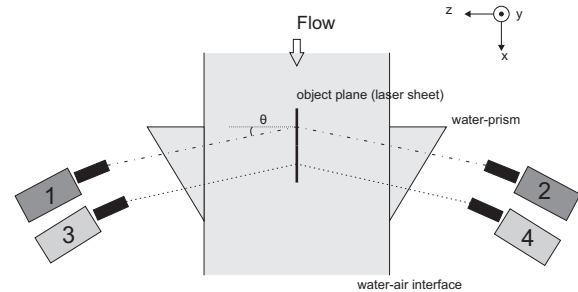


Figure 1: Top-view of the PIV setup. Note that the coordinate system is indicative only and does not represent the axes-origin.

The PCO 4000 cameras feature a large CCD array ( $4008 * 2672$  pixels<sup>2</sup>) and thus provide a large spatial dynamic range for the measurements. The originality of this experiment resides in the careful matching of this unusually large spatial dynamic range to the range of coherent structures present in the flow at that Reynolds number. This matching is achieved through:

- an optimisation of the optical magnification of the setup to resolve the small scales of turbulence.
- a reduction of the noise with a rigorous experimental procedure.
- a suitable PIV interrogation based on the Soloff method [6] and taking into account the inherent misalignment between the calibration plane and the laser sheet [5].

The resulting field of view and spatial resolution are  $[S_x; S_y] = [2.6\delta; 0.75\delta]$  and  $[l_x^+; l_y^+] = [10; 10]$ , with an interrogation window size of  $[IW_x^+; IW_y^+] = [14; 14]$ .

### DNS code

The DNS data were generated using an in-house code from Lille. The Reynolds number of the simulation is  $Re_\tau = 600$ . The flow is simulated in a symmetric (in  $z$ ) half channel of size  $[S_x; S_y; S_z] = [2.16667 * \Pi; 2; \Pi]$  with a spatial discretization of  $[N_x; N_y; N_z] = [832; 257; 384]$  points. The numerical methods use finite difference in  $x$ , spectral Fourier expansion in  $z$ , and Chebychev-collocation in  $y$ . The solution is periodized over  $2\Pi$  in  $x$ , and periodic/symmetric boundary conditions (equivalent to 'slipping' walls' conditions) are applied in  $z$ . The time integration is realised using an implicit second-order backward Euler differencing scheme.

Because of the outlet condition in  $x$ , the sub-domain situated at  $2\Pi < x < 2.16667\Pi$  should be disregarded for the analysis of the data. This is also the case for the domain at  $z < \frac{1}{8}\Pi$  and  $z > \Pi(1 - \frac{1}{8})$ , because of the slipping walls boundary condition used in  $z$ . The *useful* computational domain thus have a size of  $[S_x; S_y; S_z] = [2\Pi; 2; 6/8\Pi]$ , with  $[N_x; N_y; N_z] = [768; 257; 294]$  points.

### Comparison of the 2 datasets

The main characteristics of the two datasets are reported in table 1. Note that in order to facilitate the comparison between them, the DNS data are only studied over the half channel in  $y$  ( $N_y = 128$ ).

	$Re_\theta$	$\delta^+$	flow	$N_s$	$dt_{acq} * \frac{U_\infty}{S_x}$
SPIV	2000	1400	BL	3000	2.5
DNS	815	600	CF	50	0.1

	$x : [S_x, l_x, N_x]$	$y : [S_y, l_y, N_y]$	$z : [S_z, l_z, N_z]$
SPIV	$[2.6\delta, 10^+, 331]$	$[0.75\delta, 10^+, 94]$	none
DNS	$[2\Pi, 4.3^+, 768]$	$[1, 0.5^+/8^+, 128]$	$[\frac{6}{8}\Pi, 4.7^+, 294]$

Table 1: Characteristics of SPIV and DNS dataset

As far as the nature of the 2 turbulent flows is concerned, the measurements were taken in a zero-pressure gradient turbulent boundary layer, whereas the DNS corresponds to a fully developed turbulent channel. The comparability of those two flows have already been addressed in section 1. The Reynolds number is reported in two forms, via  $Re_\theta$  (in the boundary layer convention) and  $\delta^+$  (in the channel flow convention). Whether  $\delta^+$  or  $Re_\theta$  is considered, the DNS data are at significantly lower Reynolds number than the SPIV ones (by approx a factor 2). Besides, the ratio  $\delta^+/Re_\theta$  is checked for each type of flow. It is found to fairly close, slightly higher for the channel flow (0.74 for the CF and 0.64 for the BL), and consistent with its dependence upon the Reynolds number :

$$\frac{\delta^+}{Re_\theta} = f(C_F) = f(Re_\theta) = a * \frac{1}{Re_\theta^{1/4}}$$

The second point of interest is the spatial dynamic range of the two datasets. As expected, both the size of the velocity field and its spatial resolution are larger for the numerical data (see section 1). However, owing to CCD size of the cameras under use, the experimental spatial dynamic range remains in the same order as the numerical one in the streamwise direction. As far as the wall normal direction is concerned, the variable mesh size of the DNS offers a resolution of the viscous and buffer layers (the mesh spacing goes down to  $0.5^+$  at the wall) which remains unchallenged by the SPIV experiments. A visual representation of the relative size of the two domains is given in figure 2.

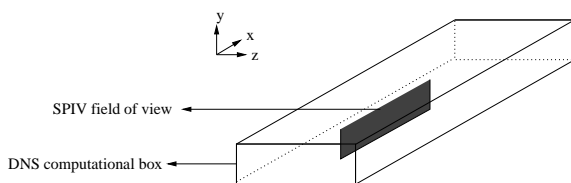


Figure 2: Schematic showing the relative size of the SPIV field of view and of the DNS computational domain

Finally, the number of realisations of the two datasets is of importance for a statistical analysis of the data. One can see that the number of sample  $N_s$  is much larger for the experiments. The degree of independence of these different realisations is conveniently reported in a non-dimensional form with the parameter  $dt_{acq} * \frac{U_\infty}{S_x}$ , where  $dt_{acq}$  is the time separating two consecutive velocity fields. A value of 1 means that the separation time is equal to the time it takes to the flow in the free-stream (or in the centerline of the channel) to move by a distance equal to the extent of the field of view (or of the computational box). The lower  $dt_{acq} * \frac{U_\infty}{S_x}$ , the higher the degree of correlation, and therefore the slower the convergence of the statistics. As expected from the difference in constraints between the two techniques (see section 1), the SPIV realisations appear thus quite independent ( $dt_{acq} * \frac{U_\infty}{S_x} = 2.5$ ) whereas the numerical data are very correlated in time ( $dt_{acq} * \frac{U_\infty}{S_x} = 0.1$ ).

### Other DNS datasets

The characteristics of two other DNS datasets from Del Alamo [8] and Moser et al [9] are also reported in table 2. They are mentioned for reference only, and will not be analysed in the present contribution.

origin	$\delta^+$	$x : [S_x, l_x]$	$z : [S_z, l_z]$
[9]	590	$[2\Pi, 9.7^+]$	$[\Pi, 4.8^+]$
[8]	550	$[8\Pi, 13^+]$	$[4\Pi, 6.7^+]$
[8]	950	$[8\Pi, 11^+]$	$[3\Pi, 5.7^+]$
[8]	1900	$[\Pi, 12^+]$	$[\Pi/2, 5.8^+]$

Table 2: Characteristics of other DNS dataset

Interestingly enough, the case Moser-590 [9] and DelAlamo-550 [8] are performed at similar Reynolds number to the Lille DNS dataset, and thus can provide two good references to our DNS dataset. Moreover, it is worth mentioning that the computational box and spatial resolution of Moser-590 [9] match well with our DNS dataset, except for the spatial resolution in  $x$  that is 2 times finer in our simulation, as a finite difference numerical scheme is used. Jimenez-950, in contrast, provide a significantly larger domain, allowing for a study of the influence of size of the velocity field. The Reynolds number of our SPIV experiments falls in between the ones of Jimenez-950 and Jimenez-1900.

### Results

This section presents some statistics computed from the SPIV and the DNS.

#### Averaging procedure employed for the statistics

As was evidenced in the previous section, the data obtained from the experiments and from the numerical simulations are of different nature, and as a result the averaging procedure employed to compute statistics on both datasets is different. Strictly speaking, an average on a quantity must be computed over a number of independent realisations. This number being rather restricted (due to limitation in storage space, CFL conditions...), a usual practice to increase the convergence of the statistics consist in averaging also over the homogeneous directions and over the time. This kind of average is not as efficient because the samples present a degree of correlation between themselves. Cousteix[17] derived, for a temporal stationary signal  $a(t)$ , a theoretical relationship to express the time  $T_a$

required for a temporal average  $a_T$  to converge to the statistical average  $\bar{a}$  within a given uncertainty  $R^2$ , as a function of an integral time scale  $\Sigma_a$  (representing the degree of correlation of  $a(t)$  over time) and of the turbulence intensity  $\bar{a}^2$ :

$$R^2 = 2 \frac{\bar{a}^2 \Sigma_a}{\bar{a}^2 T_a} \quad \text{with} \quad R^2 = \frac{(a_T - \bar{a})^2}{\bar{a}^2}$$

Quite logically, the longer  $\Sigma_a$  and the higher  $\bar{a}^2$ , the more time it takes for  $a_T$  to converge to  $\bar{a}$ . The same analysis apply to the spatial average along the homogeneous directions. It shows that the spatial and temporal average are of limited efficiency for the convergence of the turbulent quantities.

The following averaging procedure was adopted for the 2 datasets :

- DNS dataset : the time average is realised on 2 velocity fields from two time steps only. The simulation times of the two velocity fields are chosen such that the flow has completed one full passage of the computational box in the meanwhile, and the fields are thus quite independent from each other. The homogeneity of the channel flow in both x ( $N_x = 768$ ) and z ( $N_z = 294$ ) is used to average along those directions as well.
- SPIV dataset : the samples being uncorrelated in time, the quantities are naturally ensemble averaged (484 velocity fields used for the present contribution). As far as the streamwise direction is concerned, the flow being a boundary layer, it is not homogeneous in this direction. However, because of the finite extent of the field of view (165mm) with respect to the development length of the boundary layer (3500mm), the development of the boundary layer over the field of view is neglected and the quantities will also be averaged on that direction ( $N_x = 331$  points) in this contribution.

The validity of this averaging along x for the SPIV dataset has been checked by comparing mean velocity profiles obtained by averaging over the 484 samples and over an increasing number of points in x ( $N_{x_{average}} = 20, 40, 100, 200, 331$ ). The result is shown in figure 3. The same friction velocity was used to non-dimensionalize all the profiles, and was computed with the Clauser method on the case  $N_{x_{average}} = 331$ .

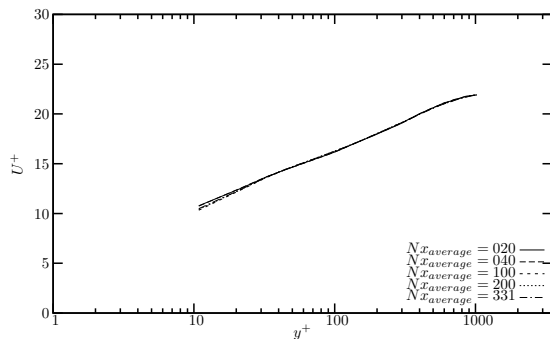


Figure 3: Test on the homogeneity of the boundary layer flow over the streamwise extent of the field of view

For  $N_{x_{average}} \geq 40$ , the mean velocity do not appear to depend anymore on the number of points used along x to compute the

mean profile. A small departure between the  $N_{x_{average}} = 20$  profile and the others can be noted in the buffer region. This can be attributed to a lack of convergence of the statistics in this region. As the peaks of rms are known to occur within that region, this is consistent with the theoretical development by Cousteix[17].

Finally, the profiles presented in this section are averaged over ( $N_y * N_x * N_z = 2 * 768 * 294 =$ )451584 points for the DNS and over ( $N_y * N_x = 484 * 331 =$ )160204 points for the SPIV. Note this overall number is smaller for the SPIV data, but that the proportion of uncorrelated points being higher, the statistics on the SPIV actually converge faster with the number of points used.

### Mean Velocity Profile

The longitudinal mean velocity profiles are shown in figure 4, in wall units. The 2 profiles show an excellent collapse in the log region, and in the higher part of the buffer layer ( $y^+ \geq 20$ ), and in the lower part of the wake ( $y^+ \leq 350$ ). Below  $y^+ = 20$ , the SPIV profile is classically biased toward higher velocities due to a lack of spatial resolution (the interrogation window size in wall units is  $14^+$ ). This bias remain relatively low compared to other studies that can be found in the literature. On a different note, the DNS profile shows an excellent resolution of the very near wall region. This is made possible thanks to an adaptative mesh size in the wall normal direction (see previous section) : the viscous sublayer and the buffer layer are resolved using 30 points in y. The departure in the outer region between the SPIV and the DNS can be accounted for by the difference in Reynolds number, or alternatively by the difference in the nature of the two flows (boundary layer/channel flow). In this plot, the friction velocity  $u_\tau$  used to non-dimensionalize the profiles have been computed in both case with the Clauser method. Since the DNS dataset show an excellent resolution down to the wall,  $u_{\tau_{DNS}}$  can also be computed through an estimation of the slope  $\frac{dU}{dy}$  at the wall. This method present the advantage of being free from the choice of numerical values for the universal constants  $K$  and  $C$  used in the log region for the Clauser method. It leads to a value of  $u_{\tau_{lin}} = 0.04884\text{m/s}$  against a value of  $u_{\tau_{log}} = 0.04956\text{m/s}$  for the Clauser method with the typical values  $K=0.41$  and  $C=5$ . The difference is only of the order of 1.5% and falls into the experimental measurement error on the velocity. It shows a very good agreement between the 2 methods.

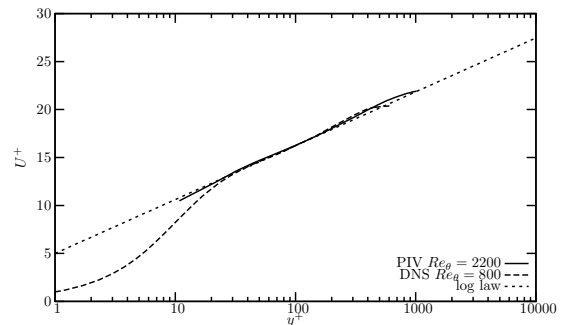


Figure 4: Mean longitudinal Velocity profile in wall units

## Spectral analysis

Spectral analysis is a tool of special interest for the analysis of turbulence which is, in essence, a multi-scale phenomenon. The spectral tensor  $\Phi_{ij}(k)$  represents the Reynolds stress density in the wave number space. Because of practical limitations on the measurements techniques, most of the experimental works have focused their interest on one-dimensionnal spectra  $E_{ij}(k_l)$  where  $l=1,2$  or  $3$ . It is defined to be twice the Fourier transform of the double spatial correlation  $R_{ij}(r_l)$ :

$$E_{ij}(k_l) = \frac{1}{\Pi} \int_{-\infty}^{\infty} R_{ij}(r_l) e^{-ik_l r_l} dr_l$$

Perry et al [14] derived similarity laws for one-dimensional spectra obtained from hot-wire anemometry, in the framework of the attached-eddy hypothesis. For a probe positioned at a height  $y$ , they identified three regions in the wave-number space where  $E_{11}$  can be non-dimensionalised with an appropriate scaling. These regions are shown in figure 5:

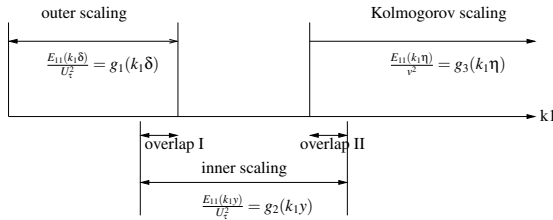


Figure 5: Different wavenumber ranges of the  $E_{11}$  spectra

From the assumption that there exist an overlap between the "outer-flow" scaling and the "inner-flow" scaling (overlap I), and between the "inner-flow" scaling and the "Kolmogorov" scaling (overlap II), two power laws can be derived for the spectra. In inner scaling it reads:

$$\frac{E_{11}(k_1 y)}{U_\tau^2} = \frac{A_1}{k_1 y}$$

$$\frac{E_{11}(k_1 y)}{U_\tau^2} = \frac{A_2}{(k_1 y)^{5/3}}$$

These regions appear as lines of slope -1 and -5/3 on log-log spectra plot in inner scaling. Region of overlap II is sometimes also called the *inertial subrange*.

Perry et al [14] indicate that the same analysis can be carried on the  $w$  motions and yields to similar results (existence of 2 regions of overlap). On the other hand, the  $v$  motions are not expected to exhibit an outer-flow scaling law, and as a result only one region of overlap (of slope -5/3) should exist in the  $E_{22}(k_1)$  spectra.

The one-dimensionnal spectra  $E_{11}(k_1)$ ,  $E_{22}(k_1)$  and  $E_{33}(k_1)$  of the SPIV and the DNS dataset were computed in the logarithmic region at  $y^+ = 100$ . They are shown on figure 6, 7 and 8 with an inner scaling. The lines of slope -1 and -5/3 are plotted as well for reference.

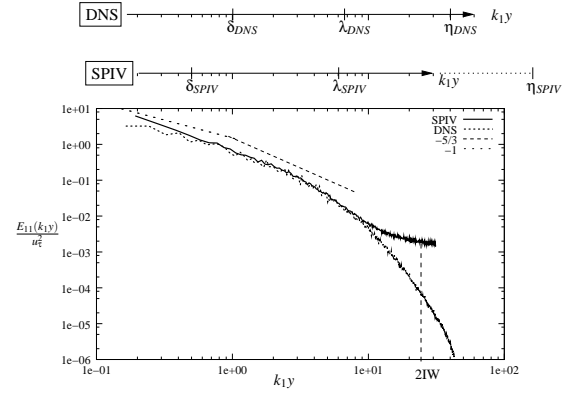


Figure 6: Longitudinal spectra of  $u$  at  $y^+ = 100$ , with an inner scaling

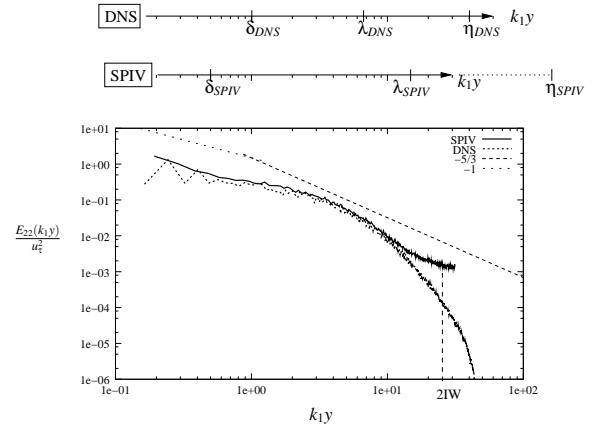


Figure 7: Longitudinal spectra of  $v$  at  $y^+ = 100$ , with an inner scaling

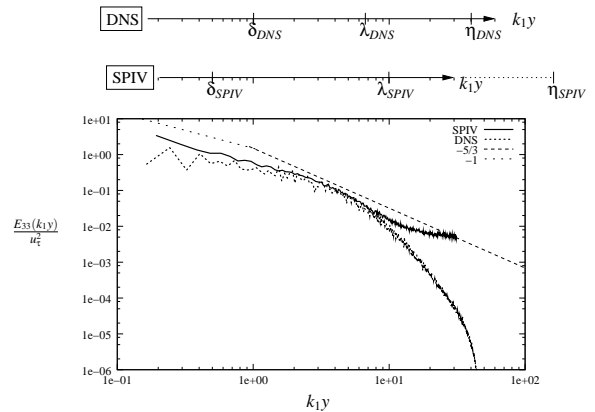


Figure 8: Longitudinal spectra of  $w$  at  $y^+ = 100$ , with an inner scaling

On top of each graph, the extent of the wavenumber domain resolved in each dataset is shown with three lengthscales representative of different type of motions in the flow:

- the boundary layer thickness  $\delta$ , for the large-scale, energy containing motions,
- the Taylor micro-scale  $\lambda_1$ ,  $\lambda_2$  and  $\lambda_3$  for the small and dissipative vortices, and
- the Kolmogorov lengthscale  $\eta$ , for the smallest isotropic eddies of the flow.

The Taylor micro-scales  $\lambda_1$ ,  $\lambda_2$  and  $\lambda_3$  were evaluated for each dataset from the second derivative at  $\Delta x = 0$  to the longitudinal double spatial autocorrelations  $R_{11}(\Delta x)$ ,  $R_{22}(\Delta x)$ ,  $R_{33}(\Delta x)$ . The Kolmogorov scale was evaluated from the classical assumption that the dissipation  $d$  balance the production  $p = -i\bar{v} \frac{\partial u}{\partial y}$  in the turbulent wall region.

From the inspection of these spectral wavenumber domains shown on top of figures 6, 7 and 8, a few general comments on the SPIV and on the DNS spectra can readily be made. First of all, one can see that, due to the difference in Reynolds number between the two dataset, the range of flow scales (from  $\delta$  down to  $\eta$ ) is wider for the SPIV dataset than for the DNS one. Then, thanks to the choice of an inner scaling for the wavenumbers, the non-dimensional Taylor micro-scale wavenumber is however the same for both dataset. Finally, the spatial dynamic range of the SPIV clearly filters out the Kolmogorov scales.

The study of each one-dimensional spectrum brings additional informations.

The spectra on the u motions  $E_{11}(k_1)$  is first considered. One can see that the SPIV and the DNS spectra show a good agreement on most of the wavenumber domain, except in the very high wavenumber region where the PIV spectra lift up from the DNS one. The two datasets show an excellent collapse in the inertial subrange. The expected slope of -5/3 is recovered. The Taylor scale of the SPIV dataset, which is a good representative of the dissipative motions, falls into that range.

At higher wavenumbers, in the so-called Kolmogorov range, the PIV spectra lift up from the DNS one. This artefact is due to the combined effects of the measurement noise and of the averaging of the velocity field over the Interrogation Window (IW) [3]. According to the Nyquist criterion, no frequency higher than half the one given by the interrogation window size can be resolved on the SPIV dataset. Indeed, one can see that the departure of the experimental spectra from the numerical one occurs at a lower wavenumber (of the order of 1/2 of the Nyquist wavenumber), under the additional effect of noise.

At lower wavenumbers, the DNS spectra match well with the -1 slope. The SPIV one, however, do not clearly exhibit such a region. This can be due to the limited size of the field of view with respect to the extent of the computational box, and in comparison with the very long extent of the uniform regions of positive and negative  $u'$  reported in the literature [16].

The spectra  $E_{33}(k_1)$  (fig.8) and  $E_{22}(k_1)$  (fig.7) can now be analysed. Both of them present the same overall behaviour as  $E_{11}(k_1)$ : very good collapse of the SPIV spectra on the DNS one from low to moderate-high wavenumbers, and then a lift-up of the SPIV spectra from the DNS one under the effect of the averaging over the IW and noise. The slope -5/3 is recovered on  $E_{33}$  and  $E_{22}$  in the inertial subrange on both dataset. On a different note from the  $E_{11}$  spectrum, a region of slope -1 is clearly visible on the  $E_{33}$  and  $E_{22}$  SPIV spectra. It is probably due to the reduced longitudinal extent of the large  $v$  and  $w$  motions

in comparison to the large  $u$ -motions, so that the extent of the SPIV field of view is actually adequate to capture them. Note that the existence of such a region on the  $E_{22}$  spectrum comes in contradiction to the theoretical development from Perry et al [14] summarised earlier in this section. As far as the DNS spectra are concerned, some spurious oscillations at low wavenumber on the  $E_{22}(k_1)$  and  $E_{33}(k_1)$  DNS spectra are visible. These oscillations denote a lack of convergence of the DNS spectra in this region.

Another remark may concern the peel-off of the SPIV spectra under the effect of noise and of the interrogation window. This phenomenon seems to occur at slightly different wavenumbers on  $E_{11}$ ,  $E_{22}$ , and  $E_{33}$ :  $k_c(E_{33}) \leq k_c(E_{11}) \leq k_c(E_{22})$ . The interrogation window size being fixed, the only explanation is that this difference in the behavior of  $E_{11}$ ,  $E_{22}$ , and  $E_{33}$  comes from different levels of noise  $\epsilon$  on  $u$ ,  $v$ , and  $w$ . Subsequently, one would get:  $\epsilon_w \geq \epsilon_u \geq \epsilon_v$ . Given the configuration of the Stereo-PIV setup detailed in section 2,  $u$  and  $v$  are the two in-plane components, and  $w$  is the out-of-plane component reconstructed mainly from differences on  $u$  measured by the two stereo cameras. The relative levels of noise on  $u$ ,  $v$ , and  $w$  deduced from the  $E_{11}$ ,  $E_{22}$ , and  $E_{33}$  spectra are consistent with the characterisation of the accuracy of stereoscopic PIV systems in Willert [18]. He established that the error on the out-of-plane component is  $\frac{1}{\tan(\theta)}$  larger than the one on the in-plane components,  $\theta$  being the stereoscopic viewing angle. Besides, he found that the two in-plane components present slightly different level of noise: the component corresponding to the direction of the image stretching (due to the stereo viewing angle) was found to be less accurate.

All the above analysis have been carried on at  $y^+ = 100$ , in the logarithmic region. One may wonder if the SPIV and the DNS spectra exhibit the same behavior in other regions of the boundary layer, especially in the buffer region and in the outer region where the mean longitudinal velocity profiles revealed some slight differences between the SPIV and the DNS datasets. The  $E_{11}(k_1)$  spectra were computed at  $y^+ = 40$ ,  $y/\delta = 0.2$  and  $y/\delta = 0.5$ . They are plotted in inner scaling in figure 9 (for the SPIV) and in figure 10 (for the DNS). A smooth have been applied to the spectra to preserve the clarity of the graphs.

On the whole, the SPIV spectra exhibit similar behavior at every wall normal positions: the slope of -5/3 is recovered in the inertial subrange, and a lift-up of the spectra is observed at high wavenumbers. A few trends of the spectra with varying wall distances can be noticed: the extent of the inertial subrange seems to increase with the wall-normal distance. Besides, the SPIV spectra at higher wall-normal positions seems to follow better the spectra obtained from DNS: the lift-up of the spectra under the effect of noise is more abrupt and occurs at higher wavenumbers relatively to the interrogation window size. This trend may indicates an increase in the size of the small vortices away from the wall.

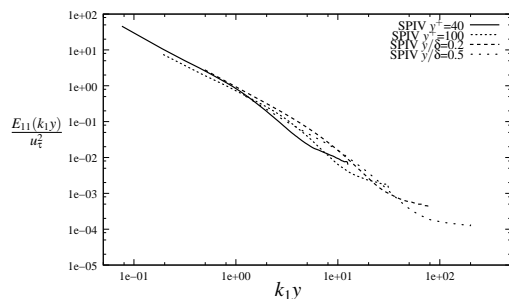


Figure 9: Longitudinal spectra of  $u$  at various wall distances with an inner scaling computed on the SPIV dataset

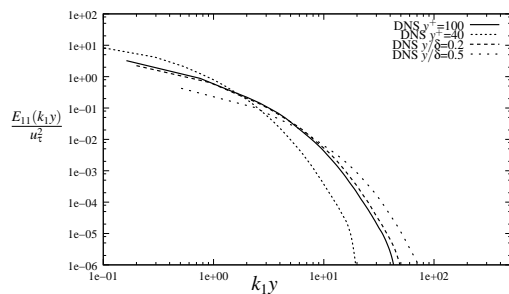


Figure 10: Longitudinal spectra of  $u$  at various wall distances with an inner scaling computed on the DNS dataset

## Conclusions

Velocity fields obtained from Stereoscopic Particle Image Velocimetry in a turbulent boundary layer and from Direct Numerical Simulations in a fully developed turbulent channel flow have been compared. In spite of differences (especially in spatial dynamic range) inherited from the working principle specificities of each technique, a spectral analysis has evidenced that the two datasets present similar behavior over a wide range of wavenumbers including the inertial sub-range. The effect of the measurement noise on the SPIV velocity spectra has been assessed, and is found to be consistent with previous characterizations of the Stereo-PIV technique accuracy.

## References

- [1] Herpin, S., Wong, C.Y. Stanislas, M. and Soria, J., High spatial resolution stereoscopic DPIV in a turbulent boundary layer, *Proceedings of the 7th international symposium on Particle Image Velocimetry*, Rome, Italy 2007.
- [2] Herpin, S., Wong, C.Y. Stanislas, M. and Soria, J., High spatial resolution stereoscopic DPIV in a turbulent boundary layer, *Submitted to Experiments in Fluids*.
- [3] Foucaut, J.M. Carlier, J. and Stanislas, M., PIV optimization for the study of turbulent flow using spectral analysis, *Measurement Science and Technology*, **15**, 2004.
- [4] Adrian, R.J., Dynamic ranges of velocity and spatial resolution of particle image velocimetry, *Measurement Science and Technology*, **8**, 1997.
- [5] Couderc, S. and Schon, J.P., Back-projection algorithm with misalignment corrections for 2D3C stereoscopic PIV, *Measurement science and technology*, **12**, 2001, 1371–1381.
- [6] Soloff, S.M. Adrian, R.J. and Liu, Z.-C., Distortion compensation for generalized stereoscopic particle image velocimetry, *Measurement science and technology*, **8**, 1997, 1441–1454.
- [7] Pope, B.P., *Turbulent flows*, 2000
- [8] Del Alamo, J.C. Jimenez, J. Zandonade, P. and Moser, R.D., Self-similar vortex clusters in the turbulent logarithmic region, *J. Fluid Mech.*, **561**, 2006, 329–358
- [9] Moser, R.D. Kim, J. and Mansour, N.N., Direct numerical simulation of channel flows up to  $Re_\tau = 590$ , *Physics of fluid*, **11**, 1999, 943–945.
- [10] Kim, J. Moin, P. and Moser, R., Turbulence statistics in fully developed channel flow at low Reynolds number, *J. Fluid Mech.*, **177**, 1987, 133–166.
- [11] Robinson S.K., Coherent motions in the turbulent boundary layer, *Annu. Rev. Fluid Mech.*, **23**, 1991, 601–639.
- [12] Wu, Y. and Christensen, K.T., Population trends of spanwise vortices in wall turbulence, *J. Fluid Mech.*, **568**, 2006, 55–76.
- [13] Moin, P. and Mahesh, K., Direct Numerical Simulation : a tool in turbulence research, *Annu. Rev. Fluid Mech.*, **30**, 1998, 539–578.
- [14] Perry, A.E. Henbest, S. and Chong, M.S., A Theoretical and experimental study of wall turbulence, *J. Fluid Mech.*, **165**, 1986, 163–199
- [15] Jimenez, J., Computing high-Reynolds-Number turbulence : will simulations ever replace experiments ?, *Journal of Turbulence*, **4**, 2003.
- [16] Hutchins, N. and Marusic, I., Evidence of very long meandering features in the logarithmic region of turbulent boundary layers, *J. Fluid Mech.*, **579**, 2007, 1–28.
- [17] Cousteix, J., *Turbulence et couche limite*, 1989.
- [18] Willert, C., Stereoscopic digital Particle Image Velocimetry for applications in wind-tunnel flows, *Measurement science and technology*, **8**, 1997, 1465–1479.
- [19] Saikrishnan, N., Marusic, I., and E.L. Longmire, Assessment of dual plane PIV measurements in wall turbulence using DNS data, *Experiments in Fluids*, **41**, 2006, 265–278.
- [20] Soria, J., Particle Image Velocimetry : Application to Turbulence Studies, in *Lectures notes on Turbulence and Coherent Structures in Fluid, Plasma and non-linear media*, chapter 7, 2006.